2026 IEEE International Conference on Robotics and Automation (ICRA 2026)
June 1-5, 2026. Vienna, Austria

Bio-inspired Rolling-Disk Continuum Robot: Logarithmic Spiral and Constant Curvature Design with Contraction Capabilities

Md Modassir Firdaus[1], Vikranth Mallru[2], Harsh Suresh Malodia[3], Madhu Vadali[1,*]

***Abstract*—Soft robotics draws inspiration from biological appendages like seahorse tails, octopus arms, and elephant trunks, which demonstrate remarkable flexibility and diverse functionalities. While advances in soft robotics have enabled delicate manipulation, safe human interaction, and medical applications, existing systems lag behind mimicking nature with a change in length. This paper presents a novel rolling-disk-based continuum robot design that replicates natural logarithmic spiral geometry while overcoming limitations of previous bio-inspired systems, including fixed length, complex elastic interconnects, and absent central lumens. The proposed 3D-printable architecture enables cost-effective rapid prototyping with adjustable parameters, achieving both logarithmic spiral and constant curvature bending, consistent with established kinematic models. A central hollow passage supports tool integration for minimally invasive procedures, while contraction capability enables dynamic length adjustment. Comprehensive mathematical analysis, CAD development, and SOFA simulations validate the design conceptualisation. Experimental demonstrations confirm bending, contraction, and grasping capabilities across diverse object geometries, establishing a foundation for scalable, adaptable tendon-driven continuum robots that bridge biological inspiration with practical engineering implementation.**

***Index Terms*—Continuum Robots, Bio-inspired, Tendon-driven Robots, Design, Spiral Bending, Constant Curvature, SOFA Framework.**

I. Introduction

Animals exhibit remarkably flexible appendages across scales from centimetre-scale prehensile tails in seahorses and chameleons [1], [2] to meter-long octopus arms and elephant trunks. [3], [4]. These structures enable diverse behaviours such as prey capture, locomotion, manipulation, and defence. This biological repertoire has strongly motivated the field of soft robotics. [5], [6], [6] Despite encouraging progress—e.g., handling delicate or irregular objects, safe human–robot interaction, [7], [8] and medical use cases [9]—engineered devices still lag natural counterparts in dexterity and speed. For instance, an elephant's trunk can gently pinch a 3 cm carrot yet hoist 300 kg logs, [10], and an octopus can reach and seize prey on sub-second timescales. [11]

The authors thank the Gujarat Council on Science and Technology for financial support. They also acknowledge feedback from the IITGN Robotics Lab team and thank IIT Gandhinagar for their ongoing support.

[1]Mechanical Engineering Department, IIT Gandhinagar, India.
[2]Computer Science and Engineering Department, IIT Bhubaneswar, India.
[3]Mechanical Engineering Department, Ahmedabad University, Ahmedabad, Gujarat, India.
*Corresponding author: madhu.vadali@iitgn.ac.in

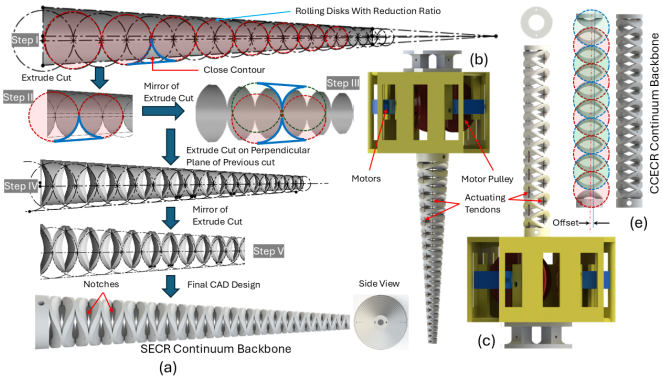

Fig. 1: (a) Rolling disk concept to CAD design, (b) Spiral Embodied Continuum Robot, (c) Constant Curvature Embodied Continuum Robot.

Bridging this gap entails three central challenges. *First,* achieving very high deformability is essential. Octopus arms, for example, can bend by nearly 180° at virtually any point along their length. [12] Many soft manipulators have been proposed with different actuation schemes, including pneumatic [13], [14] and cable-driven designs. [15], [16]. Yet most prototypes primarily realise arc-like bends with limited tip curvature, constraining conformity to small or highly varied objects. Increasing compliance via soft materials (e.g., silicone) can expand the bending range [17] but also introduces wrinkling and buckling under higher loads, undermining grasp stability. In short, softness is necessary for dexterity, but excessive softness compromises load-bearing ability.

Second, grasping strategies must explicitly leverage compliance. Exploiting passive deformation during contact can simplify control, [18], and numerous demonstrations show object acquisition with minimal sensing via wrapping [19] or "soft fingers" that envelop the target. [20] However, behaviours are often limited to a single repetitive pattern (e.g., bend–release). Grissom *et al.* presented a multi-segmented pneumatically actuated arm capable of grasping and transporting objects, [21], but, broadly, universal" strategies for reaching, grasping, and moving objects of varied shapes and from diverse poses remain scarce, whereas rigid manipulators fare better here, albeit with high planning and control complexity. Developing such general strategies is key to approaching the versatility of octopus arms.

Third, designs should be readily scalable across sizes and

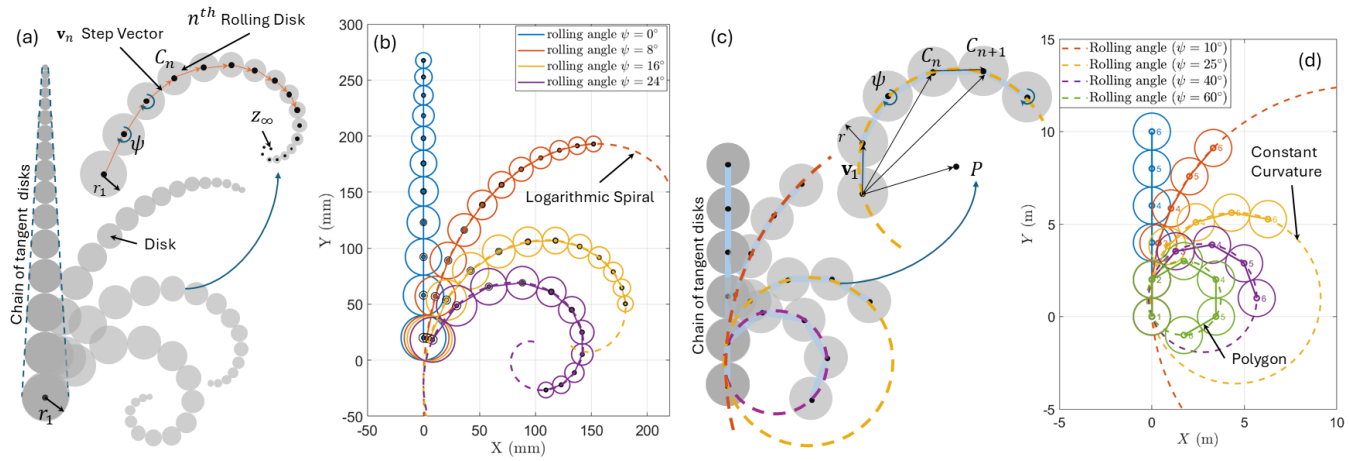

Fig. 2: (a) Rolling disk chain conceptualisation of SECR, (b) Simulation of rolling disk chain with uniform rolling angle ψ for SECR, (c) Rolling disk chain conceptualisation of CCECR, (d) Simulation of rolling disk chain with uniform rolling angle ψ for CCECR

applications. Most existing systems are tailored to specific scenarios and rely on heavy simulation coupled with trial-and-error. [22] Recent bioinspired concepts such as SpiRobs replicate the logarithmic spiral and demonstrate grasping across scales, [23] yet notable limitations persist: fixed length during contraction, elastic interconnects between bending units that complicate full 3D printing and reduce load capacity, and the absence of a central lumen, which constrains applications beyond grasping, e.g., mounting end effectors like graspers or reamers for surgical tasks.

Across species—despite substantial differences in size, anatomy (pure muscular vs. muscle–skeleton synergies), and environment (terrestrial vs. aquatic)—many appendages share a tightly packed geometry consistent with a logarithmic spiral [22], [24], [25]. Curling and uncurling are central to their function: elephants curl their trunk from the tip to pick objects off the ground, while octopuses uncurl their arms to reach. Motivated by this common geometry, our aim is to move beyond species-specific mimicry and develop a class of soft robots grounded in the logarithmic spiral, addressing limitations of SpiRobs—a novel cable-driven design that replicates this pattern in biological appendages like octopus arms and elephant trunks, enabling versatile grasping of objects varying in size by over two orders of magnitude and up to 260 times their weight, without complex feedback [21], [22], [24], [26]. SpiRobs [24] proposes a design that enables the recreation of logarithmic spiral-shaped curling and uncurling motion. The design is based on discretizing the logarithmic spiral into segments at equal angular steps from the spiral centre, generating successive polygons that, when uncurled about the central spine, produce a tapered geometry that faithfully recreates the original logarithmic spiral form. The design further demonstrates scalability across a wide range of sizes, from millimetre-scale grippers to meter-long manipulators, and operates dynamically at sub-second timescales, enabling both delicate and robust manipulation tasks across diverse environments. However, their limitations include a thin elastic layer connecting units, complicating 3D printing and reducing structural integrity; the inability to contract or adjust length; the absence of a hollow passage due to the central elastic layer, restricting use to grasping and precluding minimally invasive tools; and confinement to logarithmic spiral bending, lacking bending to other profiles like constant curvature by changing design parameters.

We introduce a rolling-disk-based architecture that naturally bends into a logarithmic spiral and, through parameter selection, achieves constant-curvature bending—a capability not shown in prior spiral-inspired systems. Because constant curvature is a standard assumption in continuum-robot kinematics, [25], [27], [28], our approach enables direct use of established models. The mechanism is fully 3D printable for rapid iteration and straightforward scaling, and it incorporates a central hollow passage to extend functionality beyond grasping—allowing tool attachment at the end effector for minimally invasive procedures [29]–[31]. We detail the design principles Figs. 1, 2 and present a bioinspired cable-driven curling/uncurling strategy in simulation in Figs. 4–6 and experimentally in Fig. 8 that exploits passive deformation to accommodate varied objects.

II. Design Methodology

The proposed design methodology exploits the kinematics of a chain of tangent circular disks that roll successively along the periphery of the preceding disk. Here, a “disk” denotes a rigid circular element in the chain, and “rolling” refers to pure rolling—contact without slip along the predecessor’s circumference. The geometric parameters, the disk radius and the rolling angle of each disk, determine the trajectory curve on which the disk centres lie, thereby defining the bending profile embodied within the continuum robot design. Input commands applied to the actuation space (i.e., tendon lengths) cause the embodied continuum backbone (CB) to conform to this predetermined bending profile. A comprehensive analysis of the resulting embodied-curve continuum robot design is presented in the subsections that follow.

A. Logarithmic Spiral Embodied Continuum Robot (SECR)

If a chain of disks exhibits varying radii with a consistent reduction ratio $k \in (0,1)$, as illustrated in Fig. 2 (a), and these disks undergo rolling motion with uniform rolling angles ψ, the geometric centers of each disk trace logarithmic spiral trajectories for each rolling angle configuration, as demonstrated in the simulation results shown in Fig. 2 (b). A proof of the geometric relationship is presented in the following analysis.

a) Disk Center Coordinates: Consider the first disk with radius $r_1 > 0$ as shown in Fig. 2 (a). The radius of the n-th disk follows the geometric sequence $r_n = r_1 k^{n-1}$, where k is the reduction ratio. Let $C_n \in \mathbb{R}^2$ represent the center of disk n, and define $\mathbf{v}_n := C_{n+1} - C_n$ as the *step* vector from center n to center $n+1$ in $\mathbb{R}^2$. The parameter $\psi \in \mathbb{R}$ denotes the constant disk rolling angle from step n to step $n+1$, with positive ψ indicating counterclockwise rotation.

Since consecutive disks are tangentially connected, the distance between their centres equals the sum of their radii:

$$d_n = \|\mathbf{v}_n\| = r_n + r_{n+1} = r_1(1+k)k^{n-1}. \tag{1}$$

The consecutive step vector $\mathbf{v}_{n+1}$ is defined in terms of the previous step vector $\mathbf{v}_n$ and the rolling angle of the $(n+1)^{\text{th}}$ disk as:

$$\mathbf{v}_{n+1} = kR(\psi)\mathbf{v}_n \tag{2}$$

where $R(\psi)$ is the planar rotation matrix, which rotates the step vector by ψ about an axis perpendicular to the plane of the rolling disk, and scales the length by k at each step. Iterating Eq. (2) gives explicit formulas:

$$\mathbf{v}_n = k^{n-1}R((n-1)\psi)\mathbf{v}_1, \tag{3}$$

and the centers accumulate as:

$$C_n = C_1 + \sum_{j=0}^{n-2} k^j R(j\psi)\mathbf{v}_1. \tag{4}$$

b) Complex Form and the Limit Point: By identifying $\mathbb{R}^2$ with the complex plane, we represent the center C_n as $z_n \in \mathbb{C}$ and the step vector $\mathbf{v}_1$ as $s_1 \in \mathbb{C}$. Eq. (4) then becomes a geometric sum:

$$z_n = z_1 + s_1 \sum_{i=0}^{n-2} (ke^{i\psi})^i = z_1 + \frac{s_1\left(1-(ke^{i\psi})^{n-1}\right)}{1-ke^{i\psi}}. \tag{5}$$

Since $0 < k < 1$, the series converges, and the chain of disk centers approaches a limit point:

$$z_\infty = \lim_{n\to\infty} z_n = z_1 + \frac{s_1}{1-ke^{i\psi}} \tag{6}$$

towards which all centers z_n converge. Subtracting (5) from (6) yields:

$$z_\infty - z_n = \frac{s_1(ke^{i\psi})^{n-1}}{1-ke^{i\psi}}. \tag{7}$$

c) Polar Coordinates and Discrete Spiral: The polar radius ρ_n and polar angle θ_n of the center C_n with respect to the limiting point z_∞ are defined as:

$$\rho_n := |z_\infty - z_n|, \qquad \theta_n := \arg(z_\infty - z_n). \tag{8}$$

The modulus and argument of (7) results in the decoupled recurrence relations:

$$\rho_{n+1} = k\rho_n, \qquad \theta_{n+1} = \theta_n + \psi \tag{9}$$

with solutions:

$$\rho_n = \rho_1 k^{n-1}, \qquad \theta_n = \theta_1 + (n-1)\psi. \tag{10}$$

Eliminating n from (10) provides an explicit relation between the radius and angle at the sampled points:

$$\rho_n = \rho_1 k^{(\theta_n-\theta_1)/\psi} = \rho_0 \exp\left(\frac{\ln k}{\psi}\theta_n\right), \rho_0 := \rho_1 e^{-(\ln k/\psi)\theta_1}. \tag{11}$$

Thus, the centers C_n lie on a logarithmic spiral, sampled at equal angular increments ψ. The simulation is shown in Fig. 2 (d).

B. Constant Curvature Embodied Continuum Robot (CCECR)

The special case of logarithmic spiral bending derived from the rolling disk is constant curvature if the reduction ratio $k = 1$, meaning each disk has the same radius as shown in Fig. 2 (c). For $r > 0$; thus centre-centre distance is given by,

$$d := \|C_{n+1} - C_n\| = r + r = 2r \qquad \forall n. \tag{12}$$

and $\mathbf{v}_n$ is given by,

$$\mathbf{v}_{n+1} = R(\psi)\,\mathbf{v}_n, \qquad \|\mathbf{v}_n\| = d. \tag{13}$$

Eqs. (3), (4) change to,

$$\mathbf{v}_n = R\big((n-1)\psi\big)\,\mathbf{v}_1;\; C_n = C_1 + \sum_{j=0}^{n-2} R(j\psi)\,\mathbf{v}_1. \tag{14}$$

a) Existence and uniqueness of a fixed point: For $\psi \not\equiv 2m\pi; m = 1, 2...$, there exist unique point $P \in \mathbb{R}^2$ such that

$$C_{n+1} - P = R(\psi)\,(C_n - P) \qquad \forall n. \tag{15}$$

Rearranging Eq. (15) gives a nonsingular linear system because $I - R(\psi)$ is invertible for $\psi \not\equiv 0 \pmod{2\pi}$:

$$P = (I - R(\psi))^{-1}(C_{n+1} - R(\psi)\,C_n). \tag{16}$$

Uniqueness follows from invertibility of $I - R(\psi)$: its eigenvalues are $1 - e^{\pm i\psi} \neq 0$ when $\psi \not\equiv 0 \pmod{2\pi}$. Eq. (15) can be written in the terms of C_1 as:

$$\begin{aligned} C_n - P &= R\big((n-1)\psi\big)\,(C_1 - P) \qquad \forall n \\ \implies \|C_n - P\| &= \|C_1 - P\| =: R_{\text{c}} \end{aligned} \tag{17}$$

Hence, all centres of the rolling disks lie on the circle of

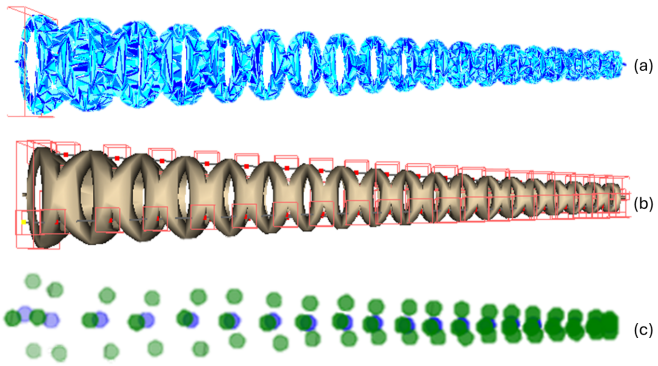

Fig. 3: (a) Volumetric mesh of the robot; (b) ROIs as small boxes at selected 3D points, moving with deformation along y-coordinates; (c) ROI average positions (green points) and extracted CB axis (blue points) via grouping at same y-coordinates.

radius R_c centred at P shown in Fig. 2 (c). Substituting $n = 1$ in Eq. (15) and using $\mathbf{v}_1 = C_2 - C_1$ we have

$$\begin{aligned} C_1 - P &= \big(R(\psi) - I\big)^{-1}\mathbf{v}_1 \\ R_c = \|C_1 - P\| &= \frac{\|\mathbf{v}_1\|}{\|e^{i\psi} - 1\|} \end{aligned} \tag{18}$$

since, $\|e^{i\psi} - 1\| = 2\|\sin(\psi/2)\|$, R_c is given by,

$$\begin{aligned} R_c &= \frac{\|\mathbf{v}_1\|}{2\|\sin(\psi/2)\|} \\ &= \frac{d}{2\sin(\psi/2)};\ (\sin(\psi/2) > 0 \text{ for } 0 < \psi < 2\pi). \end{aligned} \tag{19}$$

Thus, from Eqs. (16), (17), and (19) it is inferred that the centre of rolling of the disk chain will lie on a circle for equal rolling ψ. The simulation of a rolling disk for a reduction ratio $k = 1$ is shown in Fig. 2 (d), the centre of each rolling disk is at some circle.

III. Translating Rolling Disk to CAD

To translate the theoretical rolling disk methodology into a physically realisable model, a systematic fabrication approach has been developed based on the rolling disk design principles.

The fabrication process begins with selecting a hollow cone or tube of specified length and diameter, designated as the CB. A plane passing through the CB axis is established, along which a series of circles are drawn with an initial radius r_1 and constant reduction ratio k. The line connecting the centres of these circles defines the rolling disk axis, which is offset from the CB axis at an angle equal to the slant edge to prevent zero-thickness geometry and ensure material continuity along the CB length.

The manufacturing procedure follows a sequential approach as illustrated in Fig. 1 (a). In Step I, a closed contour is created using two tangent circles and their common tangent, forming the extrude cut profile. Step II involves creating multiple extrude cuts along the tube length, generating notches that correspond to the rolling disk diameters and

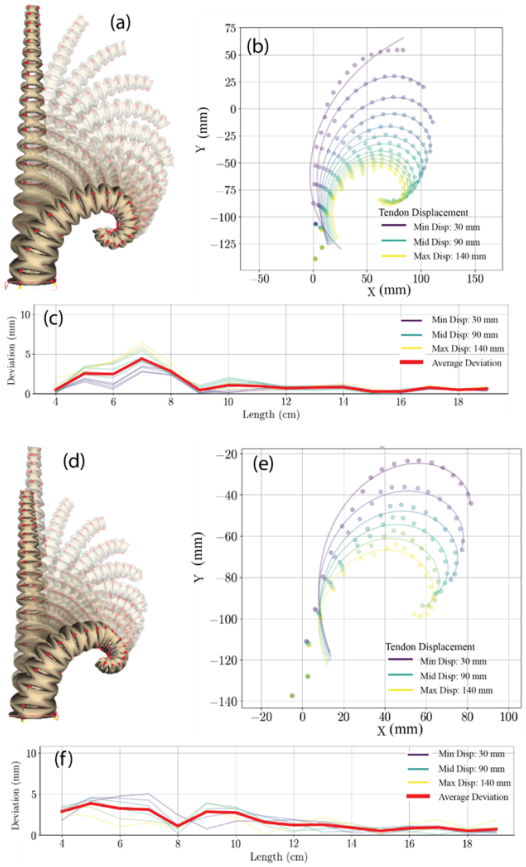

Fig. 4: (a) and (d) SECR simulation results without and with contraction, (b) and (e) Curves achieved by SECR central axis without and with contraction, (c) and (f) Deviation of SECR axis from the theoretical curve without and with contraction.

emulate the disk rolling motion for bending. These notches are subsequently mirrored to create an identical pattern on the opposite side, as shown in the zoomed view in Step III. Steps IV and V demonstrate the creation of perpendicular notch patterns by establishing a plane perpendicular to the previous extrude cut orientation. Finally, precision holes for actuating tendons are created along the periphery with equiangular distribution throughout the length, completing the final CAD design for the Spiral Embodiment Continuum Robot (SECR).

The rolling disk radius selection directly influences the achievable bending angle, where larger disk radii enable greater continuum backbone deformation by providing enlarged notches and increased deformation space. The design inherently supports contraction capability through simultaneous tendon actuation while preserving bending characteristics. When tendons are actuated, the notch geometry facilitates motion that replicates the theoretical rolling disk behavior, resulting in mechanically embodied constant curvature bending. The assembly of SECR and CCECR with actuating units are shown in Figs. 1 (b) and (c). The same method is followed to create CCECR, keeping the reduction ratio $k = 1$. Fig. 1 (e) shows the CB CAD model of CCECR

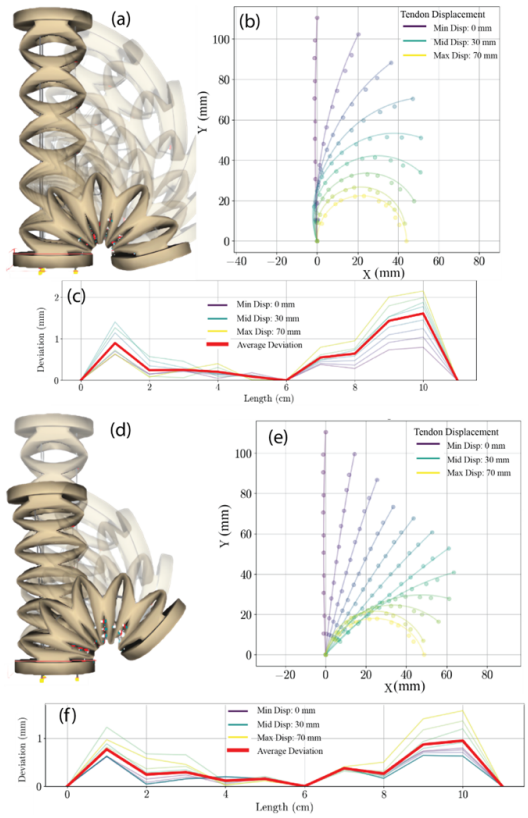

Fig. 5: (a) and (d) CCECR simulation results without and with contraction, (b) and (e) Curves achieved by CCECR central axis without and with contraction, (c) and (f) Deviation of CCECR axis from the theoretical curve without and with contraction.

IV. Design Validation Using SOFA Framework

Finite element method (FEM)-based simulations using the Simulation Open Framework Architecture (SOFA) framework [32]–[35] validate the effectiveness of the proposed SECR and CCECR designs. Fig. 3(a) presents a side-by-side comparison of the volumetric mesh and the surface mesh with overlaid regions of interest (ROI), demonstrating the internal structure and spatial distribution of the tracking regions.

Cable paths are defined as point sequences embedded in the soft material, with each cable terminating at a pull point in the volumetric mesh where tendon forces are applied. The robots are simulated using thermoplastic polyurethane (TPU-95A) with Young's modulus $E = 70\text{kPa}$ [36] and Poisson's ratio $\nu = 0.48$ [37]. All simulations employ the `ElasticMaterialObject` class [32] with `EulerImplicitSolver` for implicit time integration and `SparseLDLSolver` for efficient FEM linear system solutions, providing robust performance for large deformations and nonlinear elastic behaviour.

Multiple Regions of Interest (ROIs) are defined as small boxes at selected 3D points inside the material, as shown in Fig. 3 (b). These ROIs move with the robot during deformation. The y-coordinates run along the length of the

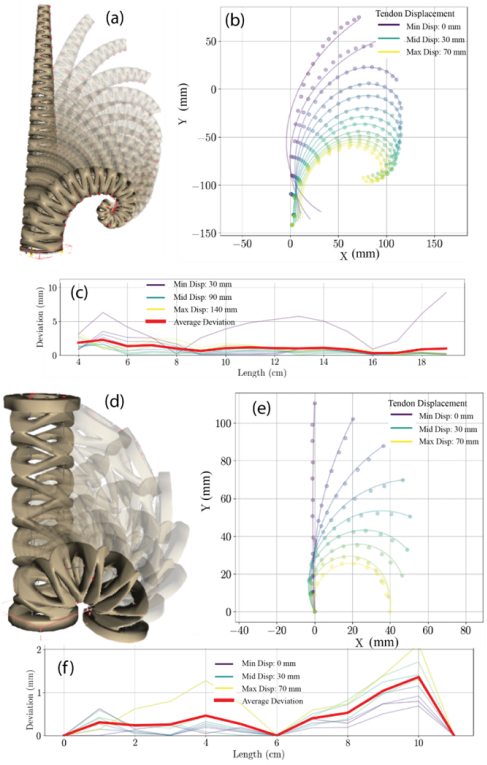

Fig. 6: SECR and CCECR simulation results in arbitrary and extrude cut planes. (a)-(c): SECR; (d)-(f): CCECR. (a,d): Bending; (b,e): Axis curves; (c,f): Bending deviations.

robot, with the placement of these ROI boxes depicted in Fig. 3 (b). For each ROI, the average position of all mesh nodes inside the box is computed at each simulation step. This computation provides a set of points that track the deformation, represented as green points in Fig. 3 (c). To extract the robot's CB axis, all ROI averages with similar y-coordinates are grouped within a specified tolerance. This grouping essentially calculates centroids for points at similar positions along the robot's length. For each group, the average coordinates of all points in that group are calculated. This calculation yields one point on the CB axis, shown as blue points in Fig. 3 (c).

To compare how well the simulated central axis with the intended geometric profiles, distinct fitting procedures are employed for the SECR and CCECR configurations. The SECR central axis is expected to conform to a logarithmic spiral. The CCECR axis should exhibit constant curvature behaviour. Singular value decomposition [38] identifies the best-fitting plane that encompasses the majority of points. This approach minimises planar deviation effectively. Points outside this plane are projected onto it to reduce the data to 2D while accounting for minor deviations. This process preserves the integrity of the main curve without a significant impact on the geometric analysis.

The center of the logarithmic spiral is estimated using bounded nonlinear least-squares optimization (L-BFGS-B) [39] applied to logarithmic residuals, initialized by data medians and refined iteratively through outlier filtering. The

SECR axis points are then parameterized into polar coordinates relative to the estimated spiral center. The spiral parameters are optimized using the Nelder-Mead simplex algorithm [40], with an iteration limit of 5,000. For the CCECR, the axis should form a circular arc, and a circle fitting procedure uses the first, middle, and last axis points to determine a circle in 3D space. Fitting accuracy is analyzed by computing absolute deviations in mm from the fitted curve for each simulation frame corresponding to a specific tendon displacement. The SOFA [32] simulation results are shown in Fig. 4 (a,d) for SECR and Fig. 5 (a,d) for CCECR, while the central axis points and fitted curve for each simulation frame are presented in Figs. 4 (b,e) for SECR and Fig. 5 (b,e) for CCECR. The deviation of each point is calculated as the shortest perpendicular distance between the fitted curve and the central axis points. For each frame, deviation versus distance from the base is plotted to visualize the profile, as shown in Figs. 4 (c,f) for SECR and Fig. 5 (c,f) for CCECR, and these profiles are averaged across frames. For the SECR, this analysis reveals an decreasing trend in deviation from base to tip, indicating that the tip position remains predictable with average deviations within 2 mm. For the CCECR, the analysis shows a similar increasing deviation toward the tip, enabling reliable prediction of the tip with average deviation within 1.5 mm. The observed deviations are attributed to a combination of factors, including material nonlinearities at the notch connections, gravitational effects, and errors introduced through spatial discretizations.

Simulation results for SECR and CCECR configurations are presented in Fig. 4 and Fig. 5, respectively. Each figure shows outcomes including the bending profile, the curve traced by the robot's central axis, and deviation from the theoretical embodied curve along the robot's length. Fig. 4 (a) and (d) depict SECR bending without and with contraction, respectively. Fig. 5 (a) and (d) show CCECR bending without and with contraction. Corresponding curves achieved by the central axis appear in Fig. 4 (b,e) and Fig. 5 (b,e). In these curve plots, the discrete points represent the extracted CB axis points, and the continuous line shows the fitted curve. Deviation analyses for the respective bending configurations are given in Fig. 4 (c,f) and Fig. 5 (c,f). The deviation plots are derived from fitting a logarithmic spiral via the Nelder-Mead algorithm for SECR cases and a circular arc for CCECR cases. These plots illustrate the distance of extracted CB axis points along the robot's length relative to the fitted curve. This analysis provides a rigorous quantitative measure of design fidelity as claimed.

To further validate the bending profile of the SECR and CCECR designs, a simulation is conducted in an arbitrary plane that does not align with the rolling disk plane used for designing the robot. The arbitrary bending plane is oriented at an angle relative to the original rolling disc plane. This configuration tests the designs' ability to maintain embodied curvature profiles in any plane under actuation. Results illustrated in Fig. 6 demonstrate low deviations from the theoretical curves. Errors decrease progressively toward the tip and further diminish as tendon displacement increases. The novel design presented in this paper demonstrates the ability of the continuum robot to bend an embodied curve in any bending plane.

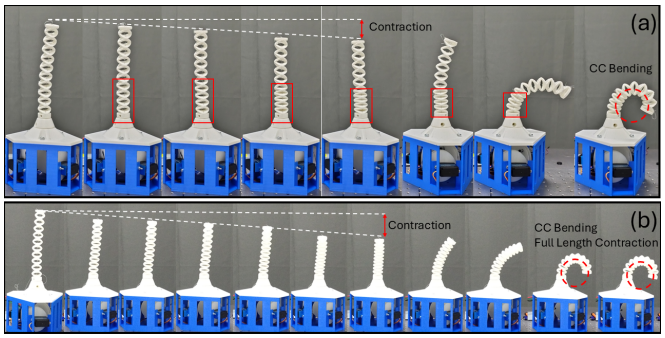

Fig. 7: Experimental Demonstration of CCECR. (a) Half-length contraction and bending, with the red box highlighting the contraction region. (b) Full-length contraction and bending.

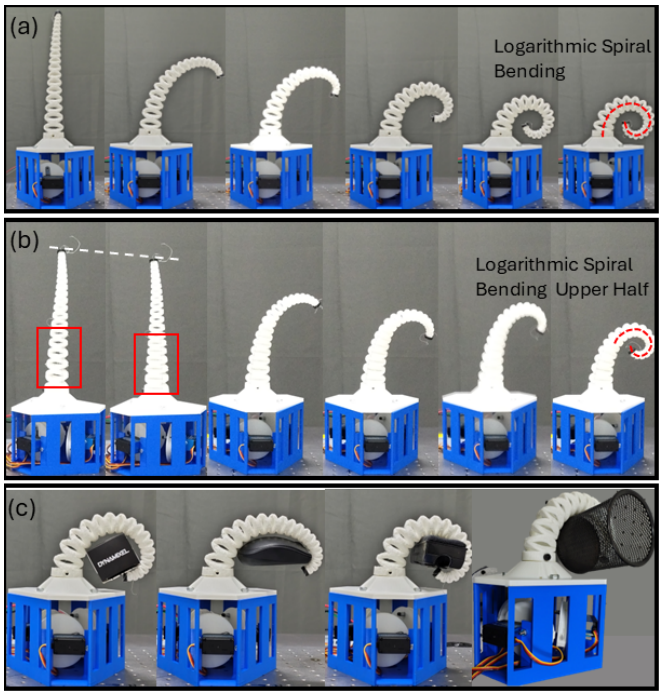

Fig. 8: Experimental Demonstration of SECR. (a) Bio-inspired spiral bending. (b) Half-length contraction and bending, with the top half exhibiting spiral bending. (c) Bio-inspired grasping, adapting to the object's geometry.

V. Experimental Setup

Two experimental setups have been developed: the CCECR and the SECR. Each configuration employs three actuating servo motors of 35 kg-cm stall torque with distinct functional roles. The primary motor provides full-length bending through a tendon that traverses the entire robot length, extending from the motor pulley to the tip, thereby enabling

bending along the length of the robot. The remaining two motors facilitate contraction to the robot through tendons that terminate at either half-length or full-length positions, depending on the desired contraction characteristics. These two contraction tendons are positioned coplanar within a single plane passing through the geometric axis of the continuum backbone.

For the CCECR configuration, both half-length and full-length contraction capabilities are targeted, with tendons mounted accordingly. Conversely, the SECR is designed for half-length contraction, with the two corresponding tendons terminating at the half-length position. Motor control is implemented using Arduino-based closed-loop position control, while the experiment operates under open-loop control.

The continuum backbones for both CCECR and SECR configurations are fabricated through 3D printing using Thermoplastic Polyurethane, while motor pulleys and chassis components are printed using PLA material. Actuation is achieved through three steel strand tendons with 0.7 mm diameter. The CCECR features a cross-sectional radius of 15 mm and a length of 200 mm, incorporating an inner hole radius of 7.5 mm and actuating tendon holes positioned 12 mm from the geometric axis. The SECR measures 248 mm in length, with the largest cross-sectional radius of 22 mm tapering to 6 mm at the smallest section, and an angle of 5.24° between the slant edges. Detailed specifications are provided in Fig. 1.

VI. Experimental Demonstrations

Five distinct experimental demonstrations have been conducted to showcase the versatile functionality of the proposed design. For the CCECR, demonstrations include half-length contraction with bending as shown in Fig. 7 (a), and full-length contraction with bending presented in Fig. 7 (b). The SECR capabilities are demonstrated through three experimental scenarios: logarithmic spiral bending illustrated in Fig. 8 (a), simultaneous contraction with bending shown in Fig. 8 (b), and full-arm grasping functionality depicted in Fig. 8 (c). Detailed analysis of each experimental demonstration is provided in the corresponding subsections.

A. Constant curvature Bending with Contraction

The contraction and bending capabilities of CCECRs are demonstrated in Fig. 7. The red box in Fig. 7 (a) highlights the contraction of the lower half-section of the CCECR, where a distinct reduction in length is clearly observable. The inclination of the white dashed line passing through the tip provides visual confirmation of this geometric change. Following complete contraction of the bottom half-section, bending actuation is applied to demonstrate the decoupled functionality. The upper half exhibits constant curvature bending with minimal influence on the contracted lower section. The slight bending observed in the lower half results from the actuating tendon traversing the entire robot length, creating a minor coupling effect between sections. In the second demonstration, as illustrated in Fig. 7 (b), full-length contraction is achieved, resulting in significantly greater overall length reduction, which is clearly evident from the position of the white dashed line. Subsequently, bending actuation is applied to the contracted configuration, producing constant curvature deformation while maintaining the shortened length profile.

B. Bio-Inspired Logarithmic Spiral Robot

The rolling disk design-based continuum robot with a constant reduction ratio $k = 0.87$ exhibits logarithmic spiral bending behavior. Fig. 8 (a) demonstrates bio-inspired logarithmic bending without contraction, where each bending configuration represents a segment of a logarithmic spiral trajectory. In Fig. 8 (b), contraction is applied to the lower half of the robot, as indicated by the red box, followed by logarithmic bending of the upper section. A distinct difference in spiral curvature characteristics can be observed between Fig. 8 (a) and Fig. 8 (b), highlighting the effect of partial contraction on the overall spiral geometry.

C. Bio-Inspired Grasping of Different Objects

The primary advantage of the logarithmic spiral configuration lies in its capability for full-arm grasping of objects with diverse geometries and dimensions. Fig. 8 (c) demonstrates the robot's grasping versatility through interaction with four distinct objects: a lightweight rectangular box, a computer mouse, a duster, and a cylindrical object. The robot exhibits excellent adaptation to curved surfaces, particularly conforming to the mouse and cylindrical profiles due to its inherent compliance. For the rectangular object, the robot effectively engages with the sharp corners through distributed contact points. The scalable nature of the design enables accommodation of various object sizes, while the contraction capability provides fine-tuned positioning for secure grasping and enhanced manipulation of smaller objects.

VII. Conclusions

This paper introduces a novel rolling-disc-based architecture for a 3D-printable continuum robot, facilitating low-cost and rapid prototyping. The design features logarithmic spiral bending with the added capability of contraction, allowing the robot to adjust its length while preserving its bending profile. A unique aspect enables a transition from logarithmic spiral to constant curvature bending by varying design parameters, addressing a gap in existing models that predominantly rely on constant curvature assumptions for kinematic analysis. Contraction is modulated by adjusting the radius of the rolling disks used to create extruded notches, enhancing the robot's adaptability. The methodology is detailed with mathematical formulations, translated into a CAD model, and validated through SOFA simulations. Experimental results demonstrate bending, contraction, combined bending with contraction, and grasping of various objects for logarithmic spiral configurations, offering a new approach to designing tendon-driven continuum robots for diverse applications.

REFERENCES

[1] M. M. Porter, D. Adriaens, R. L. Hatton, M. A. Meyers, and J. McKittrick, "Why the seahorse tail is square," *Science*, vol. 349, no. 6243, p. aaa6683, 2015.

[2] A. M. Luger, A. Ollevier, B. De Kegel, A. Herrel, and D. Adriaens, "Is variation in tail vertebral morphology linked to habitat use in chameleons?" *Journal of Morphology*, vol. 281, no. 2, pp. 229–239, 2020.

[3] W. M. Kier and M. P. Stella, "The arrangement and function of octopus arm musculature and connective tissue," *Journal of morphology*, vol. 268, no. 10, pp. 831–843, 2007.

[4] P. Dagenais, S. Hensman, V. Haechler, and M. C. Milinkovitch, "Elephants evolved strategies reducing the biomechanical complexity of their trunk," *Current Biology*, vol. 31, no. 21, pp. 4727–4737, 2021.

[5] S. Kim, C. Laschi, and B. Trimmer, "Soft robotics: a bioinspired evolution in robotics," *Trends in biotechnology*, vol. 31, no. 5, pp. 287–294, 2013.

[6] D. Rus and M. T. Tolley, "Design, fabrication and control of soft robots," *Nature*, vol. 521, no. 7553, pp. 467–475, 2015.

[7] H. Jiang, Z. Wang, Y. Jin, X. Chen, P. Li, Y. Gan, S. Lin, and X. Chen, "Hierarchical control of soft manipulators towards unstructured interactions," *The International Journal of Robotics Research*, vol. 40, no. 1, pp. 411–434, 2021.

[8] Q. Guan, F. Stella, C. Della Santina, J. Leng, and J. Hughes, "Trimmed helicoids: an architectured soft structure yielding soft robots with high precision, large workspace, and compliant interactions," *npj Robotics*, vol. 1, no. 1, p. 4, 2023.

[9] J. Burgner-Kahrs, D. C. Rucker, and H. Choset, "Continuum robots for medical applications: A survey," *IEEE transactions on robotics*, vol. 31, no. 6, pp. 1261–1280, 2015.

[10] Y. Liu, Z. Ge, S. Yang, I. Walker, and Z. Ju, "Elephant's trunk robot: An extremely versatile under-actuated continuum robot driven by a single motor," *Journal of Mechanisms and Robotics*, 2019.

[11] P. Costes, J. Soppelsa, C. Houssin, G. Boulinguez-Ambroise, C. Pacou, P. Gouat, R. Cornette, and E. Pouydebat, "Effect of the habitat and tusks on trunk grasping techniques in african savannah elephants," *Ecology and Evolution*, vol. 14, 2024.

[12] A. Tekinalp, N. Naughton, S. H. Kim, U. Halder, R. Gillette, P. G. Mehta, W. Kier, and M. Gazzola, "Topology, dynamics, and control of a muscle-architected soft arm," *Proceedings of the National Academy of Sciences*, vol. 121, no. 41, p. e2318769121, 2024.

[13] W. Dou, G. Zhong, J. Cao, Z. Shi, B. Peng, and L. zhong Jiang, "Soft robotic manipulators: Designs, actuation, stiffness tuning, and sensing," *Advanced Materials Technologies*, vol. 6, 2021.

[14] Z. Xie, F. Yuan, J. Liu, L. Tian, B. Chen, Z. Fu, S. Mao, T. Jin, Y. Wang, X. He, *et al.*, "Octopus-inspired sensorized soft arm for environmental interaction," *Science Robotics*, vol. 8, no. 84, p. eadh7852, 2023.

[15] E. Coevoet, A. Escande, and C. Duriez, "Optimization-based inverse model of soft robots with contact handling," *IEEE Robotics and Automation Letters*, vol. 2, no. 3, pp. 1413–1419, 2017.

[16] T. Morales Bieze, A. Kruszewski, B. Carrez, and C. Duriez, "Design, implementation, and control of a deformable manipulator robot based on a compliant spine," *The International Journal of Robotics Research*, vol. 39, no. 14, pp. 1604–1619, 2020.

[17] S. Nikravesh, D. Ryu, and Y. Shen, "Instabilities of thin films on a compliant substrate: Direct numerical simulations from surface wrinkling to global buckling," *Scientific Reports*, vol. 10, 2020.

[18] J. Zhu, Z. Chai, H. Yong, Y. Xu, C. Guo, H. Ding, and Z. Wu, "Bioinspired multimodal multipose hybrid fingers for wide-range force, compliant, and stable grasping." *Soft robotics*, 2022.

[19] C.-M. Chang, L. Gerez, N. Elangovan, A. G. Zisimatos, and M. Liarokapis, "On alternative uses of structural compliance for the development of adaptive robot grippers and hands," *Frontiers in Neurorobotics*, vol. 13, 2019.

[20] Z. Zhang, X. Wang, D. Meng, and B. Liang, "Bioinspired spiral soft pneumatic actuator and its characterization," *Journal of Bionic Engineering*, vol. 18, no. 5, pp. 1101–1116, 2021.

[21] I. Zournatzis, S. Kalaitzakis, and P. Polygerinos, "Softer: a spiral soft robotic ejector for sorting applications," *IEEE Robotics and Automation Letters*, vol. 8, no. 11, pp. 7098–7105, 2023.

[22] Z. Wang and N. M. Freris, "Exploiting frictional effects to reproduce octopus-like reaching movements with a cable-driven spiral robot," in *2024 IEEE 7th International Conference on Soft Robotics (RoboSoft)*. IEEE, 2024, pp. 537–542.

[23] S. Sugiura, J. Unde, Y. Zhu, and Y. Hasegawa, "High-strength and flexible mechanism for body weight support," *ROBOMECH Journal*, vol. 10, no. 1, p. 16, 2023.

[24] Z. Wang, N. M. Freris, and X. Wei, "Spirobs: Logarithmic spiral-shaped robots for versatile grasping across scales," *Device*, vol. 3, no. 4, 2025.

[25] M. M. Firdaus and M. Vadali, "Virtual tendon-based inverse kinematics of tendon-driven flexible continuum manipulators," in *Proceedings of the 2023 6th International Conference on Advances in Robotics*, 2023, pp. 1–5.

[26] Z. Wang, G. Wang, X. Chen, and N. M. Freris, "Kinematic modeling and control of a soft robotic arm with non-constant curvature deformation," in *2024 IEEE International Conference on Robotics and Automation (ICRA)*. IEEE, 2024, pp. 12 749–12 755.

[27] H. Zhang, M. Giamou, F. Marić, J. Kelly, and J. Burgner-Kahrs, "Cidgikc: Distance-geometric inverse kinematics for continuum robots," *IEEE Robotics and Automation Letters*, vol. 8, pp. 7679–7686, 2023.

[28] R. J. Webster III and B. A. Jones, "Design and kinematic modeling of constant curvature continuum robots: A review," *The International Journal of Robotics Research*, vol. 29, no. 13, pp. 1661–1683, 2010.

[29] J. Wang, C. Hu, G. Ning, L. Ma, X. Zhang, and H. Liao, "A novel miniature spring-based continuum manipulator for minimally invasive surgery: Design and evaluation," *IEEE/ASME Transactions on Mechatronics*, vol. 28, no. 5, pp. 2716–2727, 2023.

[30] J. Zhang, G. Li, T. Su, X. Liang, and Z.-G. Hou, "Design and modeling of a spring-based continuum manipulator for minimally invasive surgery," in *2024 IEEE International Conference on Robotics and Biomimetics (ROBIO)*. IEEE, 2024, pp. 565–570.

[31] F. Iqbal, M. Esfandiari, G. Amirkhani, H. Hoshyarmanesh, S. Lama, M. Tavakoli, and G. Sutherland, "Continuum and soft robots in minimally invasive surgery: A systematic review," *IEEE Access*, 2025.

[32] F. Faure, C. Duriez, H. Delingette, J. Allard, B. Gilles, S. Marchesseau, P.-J. Bensoussan, F. Poyer, M. Stengel, H. Talbot, *et al.*, "Sofa: A multi-model framework for interactive physical simulation," in *Soft Tissue Biomechanical Modeling for Computer Assisted Surgery*. Springer, 2012, pp. 283–321.

[33] I. L. Defrost Team, "Softrobots plugin for sofa," https://github.com/sofa-framework/SoftRobots, 2025, accessed: 2025-07-08.

[34] ——, "Stlib: Soft robotics toolkit library for sofa," https://github.com/sofa-framework/STLIB, 2025, accessed: 2025-07-08.

[35] E. Coevoet, T. Morales-Bieze, F. Largilliere, Z. Zhang, M. Thieffry, M. Sanz-Lopez, B. Carrez, D. Marchal, O. Goury, J. Dequidt, and C. Duriez, "Software toolkit for modeling, simulation, and control of soft robots," *Advanced Robotics*, vol. 31, no. 18, pp. 1208–1224, 2017, softRobots extension for SOFA, applied to elastic material simulations and solver configurations. [Online]. Available: https://www.sofa-framework.org/applications/publications/

[36] Ultimaker, "Ultimaker tpu 95a technical data sheet," Tech. Rep., April 2022, version 5.00. [Online]. Available: https://um-support-files.ultimaker.com/materials/2.85mm/tds/TPU-95A/Ultimaker-TPU95A-TDS-v5.00.pdf

[37] Y.-X. Xu and J.-Y. Juang, "Measurement of nonlinear poisson's ratio of thermoplastic polyurethanes under cyclic softening using 2d digital image correlation," *Polymers*, vol. 13, no. 9, p. 1498, 2021. [Online]. Available: https://www.mdpi.com/2073-4360/13/9/1498

[38] G. H. Golub and C. Reinsch, "Singular value decomposition and least squares solutions," *Numerische Mathematik*, vol. 14, no. 5, pp. 403–420, 1970.

[39] A. E. Aldridge, "Refined methods for estimating spirals and spiral deviations," *Palaeontologia Electronica*, vol. 23, no. 2, p. a41, 2020. [Online]. Available: https://palaeo-electronica.org/content/2020/3135-estimating-spirals

[40] J. C. Lagarias, J. A. Reeds, M. H. Wright, and P. E. Wright, "Convergence properties of the nelder-mead simplex method in low dimensions," *SIAM Journal on Optimization*, vol. 9, no. 1, pp. 112–147, 1998.